



Research paper

CO₂ hydrogenation to methanol over Pd/In₂O₃: effects of Pd and oxygen vacancy

Ning Rui^a, Zongyuan Wang^a, Kaihang Sun^a, Jingyun Ye^a, Qingfeng Ge^{a,b},
Chang-jun Liu^{a,*}

^a Tianjin Co-Innovation Center of Chemical Science & Engineering, School of Chemical Engineering and Technology, Tianjin University, Tianjin 300072, China

^b Department of Chemistry and Biochemistry, Southern Illinois University, Carbondale, IL 62901, USA

ARTICLE INFO

Article history:

Received 19 March 2017

Received in revised form 21 June 2017

Accepted 22 June 2017

Available online 23 June 2017

Keywords:

Methanol

Carbon dioxide

Oxygen vacancy

Indium oxide

Palladium

Hydrogenation

ABSTRACT

CO₂ hydrogenation to methanol has attracted increasing attention. Previous theoretical study suggested that Pd/In₂O₃ has a high activity for CO₂ hydrogenation to methanol with the Pd-In₂O₃ interfacial sites being the active ones. However, the strong interaction between Pd and In₂O₃ during the catalyst preparation leads to the formation of Pd-In bimetallic species and, consequently, reduces methanol yield. In this work, the Pd/In₂O₃ catalyst was prepared by firstly mixing In₂O₃ powder with Pd/peptide composite, which was followed by thermal treatment to remove the peptide. The resulting Pd/In₂O₃ catalyst is In₂O₃ supported highly-dispersed Pd-nanoparticles exposing predominately the (111) facets with particle sizes of 3.6 nm. Such Pd nanoparticles have a better ability to dissociatively adsorb hydrogen, thereby supplying hydrogen for the hydrogenation steps and facilitating oxygen vacancy creation. The interfacial sites are also active for enhanced CO₂ adsorption and hydrogenation. All these factors contribute to a superior performance of the Pd/In₂O₃ catalyst for CO₂ hydrogenation to methanol with a CO₂ conversion >20% and methanol selectivity >70%, corresponding to a STY up to 0.89 g_{MeOH} h⁻¹ g_{cat}⁻¹ at 300 °C and 5 MPa.

© 2017 Elsevier B.V. All rights reserved.

1. Introduction

The elevation of carbon dioxide level in the atmosphere has been shown to contribute to extreme climate and global warming. With the development of renewable energy, CO₂ capture and utilization have the potential to alleviate the elevated CO₂ level, and therefore, have attracted growing attention recently [1–3]. Among various options for CO₂ conversion and utilization, CO₂ hydrogenation to methanol has been considered as the favorite [4,5] since methanol can be easily transported and used as fuel or as an intermediate to produce valuable chemicals [6]. Intense research effort has been made towards CO₂ hydrogenation to methanol. However, the challenge remains to achieve a high methanol yield (high conversion and high selectivity) because of the chemical inertness of CO₂ [7–9].

The ternary Cu-ZnO-Al₂O₃ (CZA) catalysts are currently employed for methanol synthesis from mixed syngas (CO/CO₂/H₂) in industry. However, these catalysts suffer from limited activity and low selectivity because of the competing reverse water–gas shift (RWGS) reaction [10] and the inhibiting effect of water [11].

Novel catalysts with improved activity and selectivity for methanol formation are needed if CO₂ hydrogenation to methanol is to become one of the major contributors to CO₂ utilization [12–14]. In this regard, we predicted that In₂O₃ with oxygen vacancy possesses a high selectivity towards CO₂ hydrogenation to methanol based on density functional theory (DFT) studies [15,16]. DFT studies showed that the reaction follows a mechanism comprising the cyclic creation and annihilation of oxygen vacancies [16,17]. Subsequent experimental studies [4,18] of CO₂ hydrogenation on the In₂O₃-based catalysts to methanol confirmed the prediction of the DFT study. A high methanol selectivity can be achieved (55% on commercial In₂O₃ [4] and 100% on synthesized In₂O₃ [18]). However, the methanol yield over these In₂O₃ catalysts remains low due to the relatively low CO₂ conversion. To further improve the activity of In₂O₃-based catalysts, we examined the Pd/In₂O₃ catalyst for CO₂ hydrogenation based on a DFT study [19]. The DFT study predicted that the presence of Pd should improve the catalytic performance by providing metal sites for H₂ dissociative adsorption and interfacial sites for CO₂ adsorption and hydrogenation. Although the combined DFT and microkinetic study suggested that the Pd/In₂O₃ catalyst will be an excellent catalyst for methanol production from CO₂ hydrogenation [19], subsequent experimental studies showed that the strong interaction between Pd and In₂O₃ resulted in Pd-In

* Corresponding author.

E-mail address: ughg.cjl@yahoo.com (C.-j. Liu).

bimetallic species during catalyst reduction, thereby, altered the nature of interfacial sites and contributed to a poor methanol yield [20]. H_2 chemisorption study revealed that the Pd-In have less active sites for H_2 chemisorption than Pd [20]. In order to improve the methanol yield over the Pd/ SnO_2 catalyst, one has to minimize the Pd-In formation on SnO_2 supported Pd. It has been reported that the temperature of H_2 treatment affects the formation of Pd-In with limited controllability [21,22]. Therefore, novel method that prevents the formation of Pd-In alloy during preparation is needed. Recently, peptide templates have been exploited in the preparation of highly dispersed metal catalysts owing to their specific binding with the metallic surfaces and their ability of self-assembling [23]. By employing peptide templates, the size and facet of resulting catalysts can be controlled under mild conditions [23,24].

In this work, we used the peptide to assist in the preparation of the Pd/ SnO_2 catalysts. First, we prepared Pd/peptide composite using room temperature electron reduction with argon glow discharge as a cheap and simple electron source [24–26]. The reason for choosing room temperature electron reduction is that the peptide is a thermally and chemically sensitive biomaterial. Electron reduction will lead to a rapid nucleation with a slow crystal growth at room temperature, resulting in a highly dispersed metal nanoparticles (NPs) stabilized by peptide [24–26]. The resulting Pd NPs in the Pd/peptide composite featured mainly the (111) facet. The resulting Pd/peptide composite was then mixed with SnO_2 prior to the thermal treatment to remove the peptide and obtain the Pd/ SnO_2 catalyst. Such a preparation method leads to a Pd/ SnO_2 with limited Pd- SnO_2 interaction and enhanced activity for CO_2 hydrogenation to methanol.

2. Experimental

2.1. Catalyst preparation

SnO_2 was prepared by calcining $In(OH)_3$. Indium hydroxide was precipitated from a solution started by dissolving $In(NO_3)_3 \cdot xH_2O$ (Alfa Aesar, 99.999%) in deionized water, followed by the addition of excess amount of NH_4OH . The resulting slurry was aged at $80^\circ C$ for 60 min. The precipitate was then washed with deionized water and ethanol and collected by filtration. The resulting solid was dried at $60^\circ C$ for 12 h prior to calcination in static air at $350^\circ C$ for 3 h.

The Pd-peptide composite was prepared by placing the nitric acid solution of palladium nitrate hydrate (2 mM, Alfa Aesar; 99.8%) with L-Phenylalanyl-L-phenylalanine (FF) (1 mM, Shanghai Yuanye Biological Technology Co. Ltd., China; 98.0%) in the discharge chamber for electron reduction for 10 min at the room temperature. The details of the electron reduction have been previously reported [24–27]. The resulting sample, assigned as Pd-P, was collected after three times washing with deionized water. As discussed below, the resulting Pd-P composite exists in the form of a thin film. The content of Pd is 45 wt.%.

The Pd-P composite in solution was then mixed with the prepared indium oxide under stirring and left standing at room temperature for 48 h before being dried at $110^\circ C$ for 2 h. The dried sample was calcined in air at $350^\circ C$ for 0.5 h to remove the peptide. The calcination temperature, at which the peptide was completely removed, was determined by a thermal gravimetric analyzer (TGA). Prior to the catalytic activity test, the catalyst was treated in hydrogen ($H_2/N_2 = 1/9$, molar ratio) at $200^\circ C$ for 1 h. The resulting catalyst was denoted as the Pd-P/ SnO_2 catalyst. For comparison, the catalyst was also prepared following the conventional method. The introduction of Pd on the SnO_2 support was carried out by the conventional incipient wetness impregnation, using palladium nitrate hydrate as the metal precursor. After aging for 12 h at room temperature, the sample was dried at $110^\circ C$ for another 12 h. The dried

sample was calcined at $350^\circ C$ for 2 h, followed by a H_2 treatment to reduce PdO. The catalyst prepared following the conventional procedure was referred as Pd-I/ SnO_2 . In the remaining discussion, Pd/ SnO_2 refers to both Pd-P/ SnO_2 and Pd-I/ SnO_2 catalysts whereas distinction will be made when it becomes necessary.

2.2. Characterization

TGA analysis was carried out under a mixed gas atmosphere (total flow: 25 mL/min; $O_2/N_2 = 1:4$, molar ratio) at a constant rate of $10^\circ C/min$, using a Netzsch STA 449 F3 system. The catalyst (approximately 10 mg) was loaded into an alumina crucible and heated from room temperature to $700^\circ C$. The Pd loading was analyzed by inductively coupled plasma–mass spectrometry (ICP-MS) on an Agilent 7700x system. According to these ICP-MS analyses, the Pd loading is 0.97 wt% for Pd-I/ SnO_2 and 0.91 wt% for Pd-P/ SnO_2 . The X-ray diffraction (XRD) patterns of the samples were recorded on a Rigaku D/Max-2500 diffractometer at a scanning speed of $4^\circ/min$ over the 2θ range of 10° – 90° . The diffractometer was equipped with a Ni filtered Cu $K\alpha$ radiation source ($\lambda = 1.54056 \text{ \AA}$). The phase was identified by comparing the diffraction patterns with the Joint Committee on Powder Diffraction Standards (JCPDSs). Scanning electronic microscopy (SEM) studies were carried out on an FEI NanoSEM 430. The Pd-P sample was observed after freeze-drying. Transmission electron microscopy (TEM) measurements were performed on a Philips Tecnai G2F20 system. The Pd-P sample was deposited on a copper grid and observed following air drying. To prepare the catalyst samples, the catalyst was suspended in ethanol and dispersed ultrasonically for 30 min. A drop of the suspension was deposited on a copper grid coated with carbon. Hydrogen temperature programmed reduction (H_2 -TPR) was conducted on a TPDRO 1100 apparatus (Thermo Finnigan, LLC). A gaseous mixture of 5% H_2 in N_2 was used as reductant at a flow rate of 30 mL/min. Before passing through a thermal conductivity detector (TCD), the gas was purified in a trap containing NaOH to remove CO_2 . 50 mg of the sample was heated from room temperature to $500^\circ C$ at a rate of $10^\circ C/min$. Temperature programmed desorption of CO_2 (CO_2 -TPD) experiments were carried out in a fixed-bed reactor to investigate the SnO_2 surface oxygen vacancy. 200 mg of sample was reduced with 10% H_2/N_2 (30 mL/min) at $200^\circ C$ for 1 h and then cooled to $50^\circ C$ under the same gas stream, followed by CO_2 adsorption at $50^\circ C$ for 2 h. The sample was then flashed with the nitrogen flow at a rate of 30 mL/min and heated from 50 to $650^\circ C$ at a rate of $5^\circ C/min$. The products were analyzed using a TCD. Raman spectra were acquired using an inVia Reflex Renishaw Raman Spectroscopy System, with 532 nm laser as the excitation source. The laser power was set at 7 mW and the integration time is 5 s. The Raman signals are normalized for further analyses. The UV–vis absorption spectra of the samples were recorded with a UV-2600 UV–vis spectrophotometer (Shimadzu Corporation). The X-ray photoelectron spectroscopy (XPS) analyses were performed with a Perkin Elmer PHI-1600 spectrometer using Mg $K\alpha$ ($h\nu = 1,486.6 \text{ eV}$) radiation. The binding energies were calibrated using the C1s peak (284.8 eV) as a reference.

2.3. Catalytic activity

The activity tests for CO_2 hydrogenation over the pure SnO_2 and Pd/ SnO_2 catalysts were conducted in a tubular micro-reactor. 0.1 g of the catalyst, mixed with 0.5 g of SiC as diluent, was loaded into the reactor. The feed of reactants ($H_2/CO_2 = 4/1$, molar ratio) was introduced to the system at a gaseous hourly space velocity (GHSV) of $21000 \text{ cm}^3 \text{ h}^{-1} \text{ g}_{cat}^{-1}$ under 5 MPa. The effluent was analyzed using an online gas chromatograph (Agilent 4890D) equipped with a two-column system connected to a flame ionized detector (FID) and a

TCD, respectively. The catalytic activities were recorded from 200 to 300 °C. The sensitivity of In_2O_3 and $\text{Pd}/\text{In}_2\text{O}_3$ catalysts to the space velocity and total pressure was determined by varying the GHSV ($\text{GHSV} = 9000, 15000, 21000, 30000, 48000 \text{ cm}^3 \text{ h}^{-1} \text{ g}_{\text{cat}}^{-1}$) and pressure ($P = 1.0, 2.0, 3.0, 4.0, 5.0 \text{ MPa}$), respectively. The CO_2 conversion (X_{CO_2}), CH_3OH selectivity ($S_{\text{CH}_3\text{OH}}$) and space time yield (STY) were calculated according to the following equations:

$$X_{\text{CO}_2} = \frac{F_{\text{CO}_2, \text{in}} - F_{\text{CO}_2, \text{out}}}{F_{\text{CO}_2, \text{in}}} \times 100\%$$

$$S_{\text{CH}_3\text{OH}} = \frac{F_{\text{CH}_3\text{OH}, \text{out}}}{F_{\text{CO}_2, \text{in}} - F_{\text{CO}_2, \text{out}}} \times 100\%$$

$$\text{STY} = \frac{F_{\text{CO}_2, \text{in}} X_{\text{CO}_2} S_{\text{CH}_3\text{OH}} M}{W}$$

where F is the molar flow rate, M is the molar mass of methanol and W is the weight of the catalyst sample.

3. Results

3.1. Catalytic activity

Fig. 1(a) and (b) shows CO_2 conversion, methanol selectivity and STY on the pure In_2O_3 and $\text{Pd}/\text{In}_2\text{O}_3$ catalysts. On all three catalysts, the CO_2 conversion increases with the increase of the reaction temperature while the selectivity of methanol decreases. However, the selectivity remains around 70% even when the reaction temperature increases to 300 °C. This confirms that the In_2O_3 -based catalysts possess high methanol selectivity in general. The decrease

in the selectivity of methanol with the increasing reaction temperature can be attributed to the competing reverse water gas shift, a major side reaction for CO_2 hydrogenation, which is thermodynamically favorable with the increasing reaction temperature [28]. Clearly, the $\text{Pd}/\text{In}_2\text{O}_3$ catalysts show much higher activity than the pure In_2O_3 catalyst at all temperatures. These results indicate that the loading of Pd NPs on In_2O_3 significantly improves the activity of In_2O_3 . It is important to highlight that CO_2 conversion is above 20% at 300 °C for the $\text{Pd-P}/\text{In}_2\text{O}_3$ catalyst with a maximum STY (Fig. 1(b)) of $0.89 \text{ g}_{\text{MeOH}} \text{ h}^{-1} \text{ g}_{\text{cat}}^{-1}$, higher than that for the $\text{Pd-I}/\text{In}_2\text{O}_3$ catalyst. In contrast, the conversion and selectivity on the Cu-Zn-Al catalyst are only around 2% and 11%, respectively, with a STY value of $0.122 \text{ g}_{\text{MeOH}} \text{ h}^{-1} \text{ g}_{\text{cat}}^{-1}$ [18]. Therefore, the catalytic performance of $\text{Pd-P}/\text{In}_2\text{O}_3$ catalyst is much higher than that of the reported Cu-based and Pd-based catalysts (as shown in Table S1, S2 and S3), making it competitive for large-scale CO_2 conversion.

The methanol selectivity can be further optimized by adjusting the GHSV to higher values, at which the RWGS reaction is further limited. For the In_2O_3 and $\text{Pd}/\text{In}_2\text{O}_3$ catalysts, when $\text{GHSV} > 21000 \text{ cm}^3 \text{ h}^{-1} \text{ g}_{\text{cat}}^{-1}$ (Fig. 1(c)), the selectivity of methanol reaches 70%. Therefore, GHSV is set here at $21000 \text{ cm}^3 \text{ h}^{-1} \text{ g}_{\text{cat}}^{-1}$ (except for the reactions with the effect of GHSV) to achieve a high methanol selectivity and avoid a low single pass conversion caused by high GHSV. In accordance with the Le Châtelier's principle, high-pressure also favors methanol as product from CO_2 hydrogenation. Further experiments at 300 °C and $21000 \text{ cm}^3 \text{ h}^{-1} \text{ g}_{\text{cat}}^{-1}$ show a linear increase of STY upon the increasing pressures (1.0–5.0 MPa; Fig. 1(d)).

We also investigated the re-usability of the In_2O_3 and $\text{Pd}/\text{In}_2\text{O}_3$ catalysts. The results are shown in Fig. 1(e). At the end of each run, the catalysts were cooled down to room temperature for the next

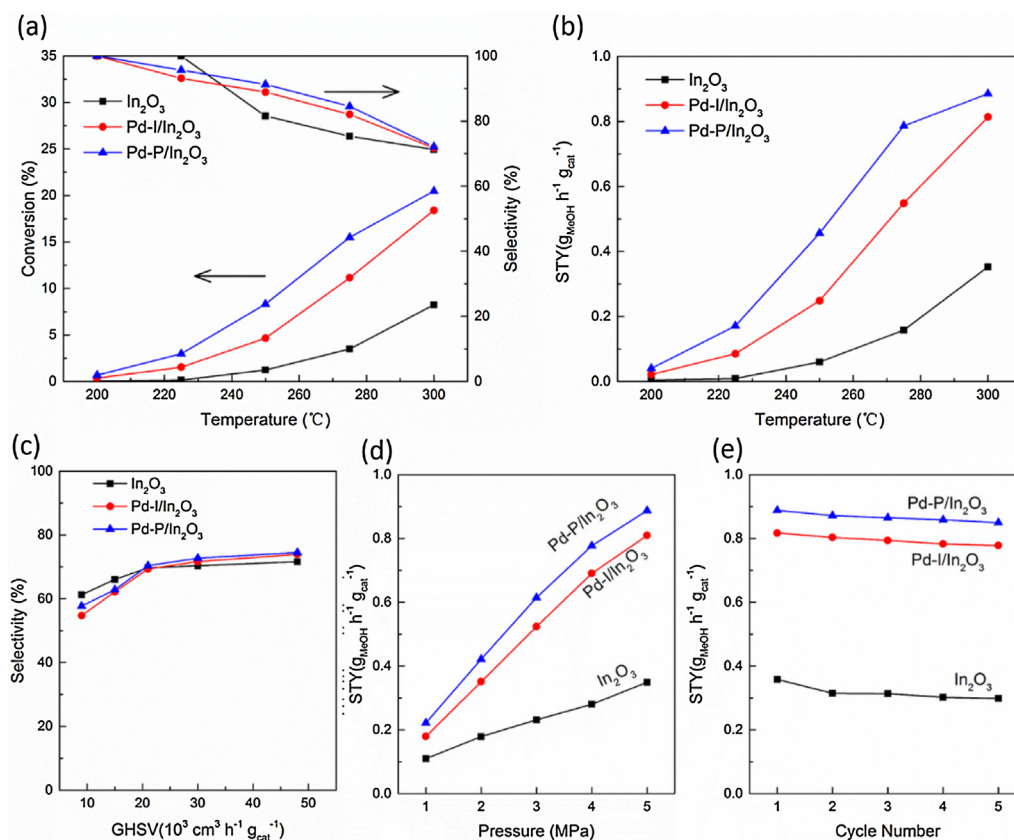


Fig. 1. (a) CO_2 conversion, methanol selectivity and (b) methanol space time yield as a function of temperature; (c) methanol selectivity as a function of the gas hourly space velocity, (d) methanol space time yield as a function of the pressure, and (e) cycle number over In_2O_3 and $\text{Pd}/\text{In}_2\text{O}_3$ catalysts. Standard reaction conditions are defined as $T = 300^\circ\text{C}$, $P = 5.0 \text{ MPa}$, and $\text{GHSV} = 21000 \text{ cm}^3 \text{ h}^{-1} \text{ g}_{\text{cat}}^{-1}$.

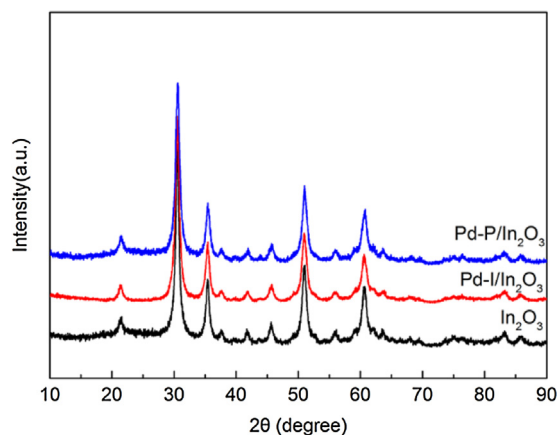


Fig. 2. XRD patterns of In_2O_3 and $\text{Pd}/\text{In}_2\text{O}_3$.

batch. A STY efficiency of $\sim 83\%$ and 95% is maintained after five runs for the In_2O_3 and $\text{Pd}/\text{In}_2\text{O}_3$ catalysts, respectively. The selectivity remains almost constant during re-usability test (not shown). These results confirm that the $\text{Pd}/\text{In}_2\text{O}_3$ catalysts are stable under the reaction conditions.

3.2. Catalyst characterization

The Pd loading of Pd-P composite and $\text{Pd}/\text{In}_2\text{O}_3$ catalysts were also assessed by TGA analysis [29]. The TGA results are shown in Fig. S1. After the TGA test, a surface oxide layer forms on the electron reduced metal Pd NPs. From the TGA results, we find that the Pd loading of the Pd-P composite and $\text{Pd}/\text{In}_2\text{O}_3$ catalysts is around 45% and 1%, respectively. The Pd loading in the $\text{Pd}/\text{In}_2\text{O}_3$ catalysts measured by TGA agrees well with the ICP-MS results (0.97 wt% for Pd-I/ In_2O_3 and 0.91 wt% for Pd-P/ In_2O_3). The calcination temperature of the $\text{Pd}/\text{In}_2\text{O}_3$ catalysts was set at 350°C according to TGA results, at which the peptide is completely removed and palladium nitrate completely decomposed.

The crystalline structure of In_2O_3 support and $\text{Pd}/\text{In}_2\text{O}_3$ catalysts is presented in Fig. 2. The In_2O_3 support only exhibits the peaks of the cubic In_2O_3 crystalline lattice (PDF#06-0416). The XRD patterns of Pd-P composite and $\text{Pd}/\text{In}_2\text{O}_3$ before H_2 treatment (assigned as

$\text{Pd}/\text{In}_2\text{O}_3\text{-BT}$) are shown in Fig. S2 (a) and (b), respectively. For the Pd-P composite and $\text{Pd}/\text{In}_2\text{O}_3$ catalysts, no characteristic diffraction peaks of Pd or PdO can be observed. This can be attributed to the fact that Pd particles are too small (below 3 nm) to be detected by XRD and/or the Pd loading is too low [26,30,31]. The XRD patterns of the catalysts after reaction (assigned as $\text{In}_2\text{O}_3\text{-AR}$ and $\text{Pd}/\text{In}_2\text{O}_3\text{-AR}$) are shown in Fig. S2(c). No metallic In was detected after the reaction, indicating the stability of the catalysts.

Fig. 3 shows SEM and TEM images of the Pd-P composite and $\text{Pd}/\text{In}_2\text{O}_3$ catalysts. TEM images in Fig. 3(a) and (b) show that typical Pd NPs prepared using incipient wetness impregnation (Pd-I/ In_2O_3), which display a mean Pd particle size of 7.4 nm (Fig. S3). The Pd NPs can be clearly identified with lattice fringes attributable to the (111) and (200) planes. In addition, Pd-In is formed and identified in the region between Pd NPs and In_2O_3 . These results indicate a strong interaction between Pd and In_2O_3 in the catalysts prepared by using the conventional approach. A zoomed-in view of the lattice fringes and the particle size distribution of Pd NPs are shown in Fig. S3.

Fig. 3(c) and (d) presents the SEM images of the top and side view of the as-prepared Pd-P composite, showing a free-standing film composed of peptide FF and Pd NPs. This morphology is consistent with the observation of $\text{A}\beta_{16-22}$ peptide self-assembled biofilm and P-Pd/ $\text{A}\beta_{16-20}$ film prepared by the electron reduction [24,25]. The photograph of the resultant composite is shown in Fig. S4. Electron reduction of Pd ions in solution directly has been attempted but no useful product is obtained. Therefore, the peptide plays an essential role in assembling the Pd NPs into a composite film.

TEM images of the Pd-P composite (Fig. 3(e) and (f)) indicates that the composite film assembled from the Pd NPs and FF monomers contains a uniform distribution of NPs throughout the film. The highly dispersed particles are the Pd NPs (as shown in HR-TEM and XPS analyses), while the size decreases to 2.0 nm (Fig. S5). This result suggests that the electron reduction and peptide help to control the size of Pd NPs. Palladium ions will bind specific sites of the peptide through electrostatic interactions between negatively charged peptide sites and positively charged Pd^{2+} [32], resulting in well-distributed Pd^{2+} ions. Furthermore, the room temperature electron reduction allows better size control by fast nucleation and slow crystal growth [33] than the convention approach. These combined effects result in the Pd nanoparticles dispersed well on the

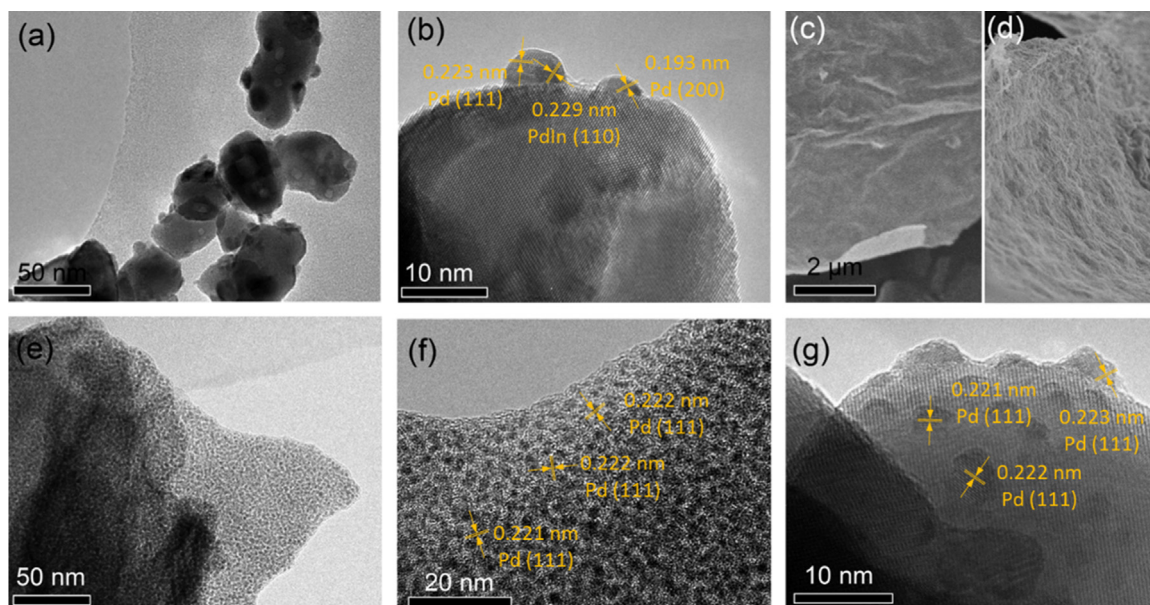


Fig. 3. TEM images of (a) and (b) Pd-I/ In_2O_3 , SEM images of (c) and (d) Pd-P composite, TEM images of (e) and (f) Pd-P composite, (g) Pd-P/ In_2O_3 .

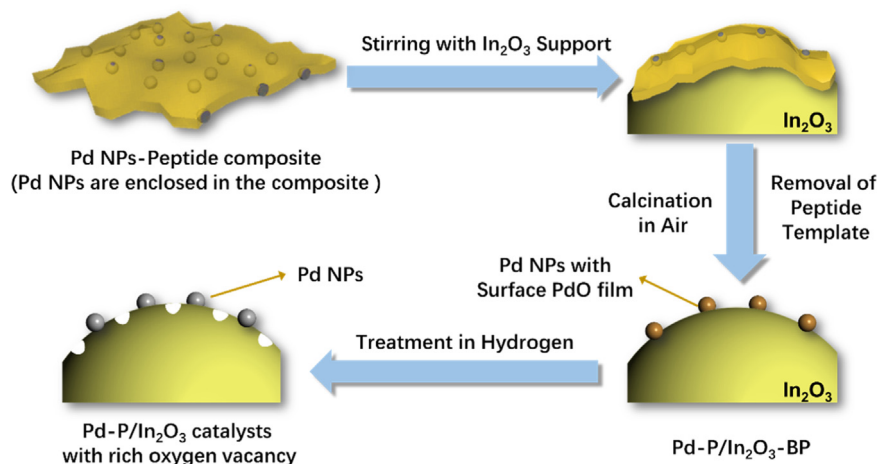


Fig. 4. Preparation procedure of Pd-P/In₂O₃ catalyst.

peptide composite [23,24]. A zoomed-in view of the lattice fringes and the size distribution of Pd NPs in Fig. 3(f) are provided in Fig. S5.

Fig. 3(g) shows the TEM image of Pd-P/In₂O₃ catalyst. We can find that the Pd NPs are dispersed well on In₂O₃, while their sizes are increased to ~3.6 nm (Fig. S6). The bigger particle size and hemispherical shape of the Pd NPs after calcination may be a result of diffusion aggregation of the smaller particles during the thermal treatment. We note the interparticle spacing is close to that in the Pd-P composite. The small size of Pd NPs in Pd-P/In₂O₃ catalysts resulted in more interfacial sites in Pd-P/In₂O₃, which are active for CO₂ adsorption and hydrogenation [19]. These results demonstrate that our synthetic strategy is efficient as the features are well preserved after the transformation of Pd NPs in Pd-P film to Pd-P/In₂O₃ catalysts. The preparation procedure of the Pd-P/In₂O₃ catalyst is illustrated in Fig. 4.

The reducibility of In₂O₃ and Pd/In₂O₃ without H₂ treatment was studied using H₂-TPR and the H₂-TPR profiles are shown in Fig. 5(a). For In₂O₃, the reduction starts at around 150 °C. Two broad peaks centered at 200 °C and 320 °C were assigned to the reduction of surface In₂O₃. These two peaks also correspond to the formation of the oxygen vacancy [18]. For Pd-I/In₂O₃, H₂-TPR gives one small peak centered at about 40 °C, which can be attributed to the reduction of PdO [34]. This peak is not present in Pd-P/In₂O₃ because Pd is already in the metallic form. Higher temperature peaks can be attributed to the reduction of In₂O₃. The TPR profiles also exhibit a negative peak on Pd/In₂O₃ catalysts at ~360 °C, corresponding to hydrogen release from the catalysts. The extra hydrogen was dissolved in the Pd lattice after the complete reduction of PdO [22]. In

addition, the onset temperature of In₂O₃ reduction is decreased to 70 °C with the peak intensity enhanced greatly with Pd. This result indicates the presence of the supported Pd helps to reduce In₂O₃ and generate oxygen vacancy, attributable to the enhanced hydrogen dissociation and spillover effect [35]. It is worth noting that Pd-P/In₂O₃ consumes more H₂ than Pd-I/In₂O₃.

The surface oxygen vacancies were further characterized using CO₂-TPD, as shown in Fig. 5(b). A single peak at approximately 80 °C for all three samples is believed to be from the physically adsorbed CO₂. For In₂O₃, the peak at about 430 °C is attributed to CO₂ adsorption in the thermally induced oxygen vacancy sites (O_{v1}), as In₂O₃ was prepared by thermal calcination without H₂ reduction. After Pd NPs are introduced to In₂O₃ and treated under H₂, an additional peak at ~320 °C appeared, which can be assigned to the oxygen vacancy formed by H₂ reduction (O_{v2}) [18]. The peak area associated with the thermal induced oxygen vacancy sites is similar for all samples. There is a significant increase in the peak associated with H₂ induced oxygen sites, indicating significantly increased density of oxygen vacancy in the Pd-P/In₂O₃ catalyst. The consequences are in good agreement with above-mentioned TPR data. Consequently, the increased oxygen vacancy sites resulted in significantly enhanced CO₂ hydrogenation reactivity.

4. Discussions

Previous DFT studies predicted that the oxygen vacancy sites and Pd/In₂O₃ interfacial sites are the active sites for selective hydrogenation of CO₂ to methanol on In₂O₃-based catalysts [16,19]. The present experimental studies showed that a high performance

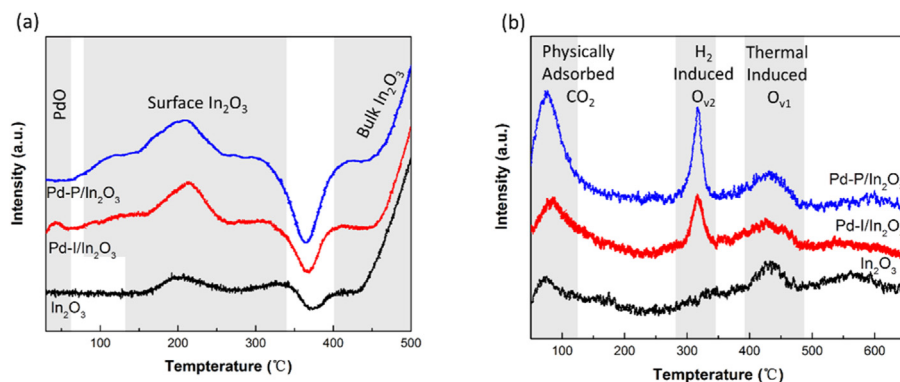


Fig. 5. (a) H₂-TPR and (b) CO₂-TPD profiles of In₂O₃ and Pd/In₂O₃.

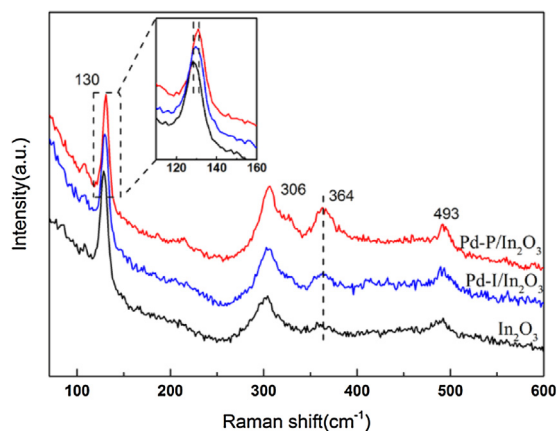


Fig. 6. Visible Raman spectra of In_2O_3 and $\text{Pd}/\text{In}_2\text{O}_3$.

$\text{Pd}/\text{In}_2\text{O}_3$ catalyst can be synthesized with the assistance of peptide. The $\text{Pd-P}/\text{In}_2\text{O}_3$ catalysts attained a high reactivity by providing both interfacial and oxygen vacancy sites for CO_2 hydrogenation without forming Pd-In alloy. The catalysts were further analyzed using room temperature visible Raman-scattering and the spectra are shown in Fig. 6.

Pd^0 is Raman inactive. All peaks in the Raman spectra belong to In_2O_3 and agree well with the reported values [36,37]. The scattering feature at 130 cm^{-1} is assigned to the In-O vibration of InO_6 units [36], while 306 cm^{-1} is attributed to the bending mode of the InO_6 octahedrons. The peak at 493 cm^{-1} is usually interpreted as the stretching vibrations of the InO_6 octahedrons [37]. The peak centered at 364 cm^{-1} is assigned to the stretching vibrations of In-O-In ($\nu(\text{In-O-In})$). As shown in Fig. 6, the intensity of the 364 cm^{-1} peak increased significantly in the presence of Pd . This can be attributed in part to the increased oxygen vacancy density by breaking one of the double oxygen bridge $\text{In}^{\text{IV}}\text{O}_2$ bonds [16,38,39]. The slightly red-shifted scattering feature located at $\sim 130\text{ cm}^{-1}$ can be attributed to the lattice expansion and mode softening due to oxygen vacancies formation [40].

Fig. 7(a) shows UV–vis absorption spectra of In_2O_3 and $\text{Pd}/\text{In}_2\text{O}_3$ catalysts. The strong UV absorption of In_2O_3 is a reflection of its semiconducting nature. The band gap can be determined from absorption spectra using the Tauc relation [41]. Based on the plot of $(\alpha h\nu)^2 \sim$ the photo energy, $h\nu$, in Fig. 7(b), a band gap of In_2O_3 is estimated to be 2.96 eV, and reduced to 2.76 and 2.55 eV for $\text{Pd-I}/\text{In}_2\text{O}_3$ and $\text{Pd-P}/\text{In}_2\text{O}_3$ catalysts, respectively. The results indicate that the oxygen vacancies shift the onset of light absorption from the UV to the visible region, due to the presence of Pd . As such, the increase in visible light absorption can be attributed to the electronic transition from the In_2O_3 valence band to the newly created

oxygen vacancy level, or from the oxygen vacancy level to the conduction band [42,43]. The sensitivity of light absorption to oxygen vacancy in In_2O_3 makes $\text{Pd}/\text{In}_2\text{O}_3$ potentially useful in exploiting visible light for photocatalysis.

XPS is employed to characterize the chemical environment of In , O , and Pd species of the catalysts in Fig. 8. Full-range XPS spectra are shown in Fig. S7. The $\text{In } 3\text{d}$ core level spectra in Fig. 8(a) show two peaks located at 444.2 and 451.8 eV, which can be attributed to the characteristic spin-orbit split $3\text{d}_{5/2}$ and $3\text{d}_{3/2}$ [44], indicating the indium valence is mainly +3 for all samples. The $\text{O } 1\text{s}$ core level spectra are shown in Fig. 8(b), clearly showing two peaks after deconvolution. The peak at about 529.7 eV originates from the oxygen in In-O-In ($\text{O}_{\text{lattice}}$), and the peak at 531.6 eV corresponds to the oxygen defects in the metal oxide support (O_{defect}) [18,39]. The peak area (A) of different oxygen species is used to estimate the relative concentrations of surface oxygen vacancy (C_{Odefect}) based on the formula $C_{\text{Odefect}} = A_{\text{Odefect}} / (A_{\text{Odefect}} + A_{\text{O}_{\text{lattice}}})$. The results are 44.2% for In_2O_3 , 55.3% for $\text{Pd-I}/\text{In}_2\text{O}_3$, and 63.4% for $\text{Pd-P}/\text{In}_2\text{O}_3$. Fig. 8(c) showed the plot of the STY of methanol at 250°C as a function of the relative oxygen vacancy concentration. In these studies, the CO_2 conversion was controlled to be lower than 10% by reaction temperature in order to eliminate the impact of external diffusion. Catalysts used for activity tests are powder. The internal diffusion is thereby negligible. Hence, the STY of methanol reflects the catalytic activity with no diffusion influence. Obviously, the STY of methanol is larger when the catalyst has the higher number of active sites. For $\text{Pd-P}/\text{In}_2\text{O}_3$ catalysts, the rapid increase of STY may be attributed to both the high oxygen vacancy density and more interfacial sites.

The intensity of $\text{Pd } 3\text{d}$ profiles of $\text{Pd}/\text{In}_2\text{O}_3$ catalysts in Fig. 8(d) is weak because of the low Pd loading. However, two peaks are still clearly identified. The binding energy values confirm that Pd NPs on In_2O_3 surface are in Pd^0 state [45]. Besides, the XPS spectra of $\text{Pd } 3\text{d}$ in $\text{Pd}/\text{In}_2\text{O}_3\text{-BT}$ are shown in Fig. S8(a). All peaks move to higher energy compared to the reduced ones because of the existence of PdO . For $\text{Pd-I}/\text{In}_2\text{O}_3\text{-BT}$, palladium is detected only in the form of PdO , which is confirmed by binding energy value of 337.2 eV [46]. This is derived from the calcination of palladium nitrate. While, as to $\text{Pd-P}/\text{In}_2\text{O}_3\text{-BT}$ samples, although Pd is in the metallic state in Pd-P composite film, the surface oxide layer, formed in air while removing the peptide, inhibits the further oxidation of Pd NPs [47] and contributes to the binding energy shift. This hypothesis is confirmed by the XPS analyses (Fig. S8(b)), with which the peptide is removed under N_2 to protect the surface palladium from oxidation. The $3\text{d}_{5/2}$ peak locates at 335.5 eV (regarded as standard binding energy of Pd^0 state) confirms the metallic state. We noted a 0.2 eV shift (335.7 eV of the reduced samples) to higher binding energy after H_2 treatment. Besides, it must be also mentioned that the $\text{Pd } 3\text{d}_{5/2}$ peak of $\text{Pd-I}/\text{In}_2\text{O}_3$ is located at 336.1 eV, shifted to a higher energy (0.6 eV) compared to the standard binding energy

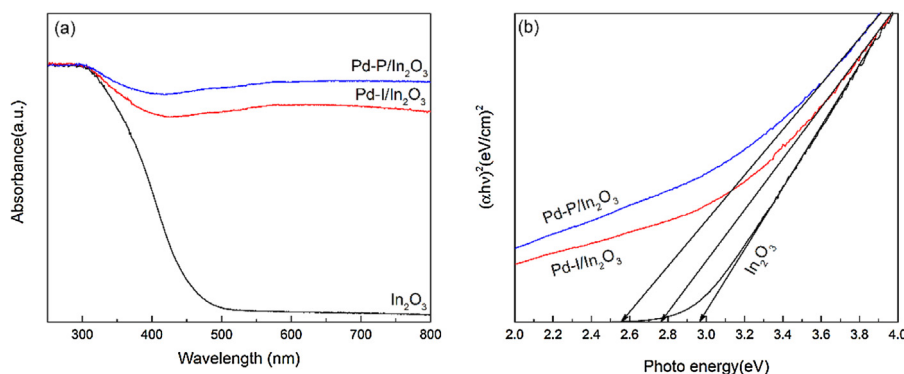


Fig. 7. (a) UV–vis absorption spectra and (b) Tauc plot of In_2O_3 and $\text{Pd}/\text{In}_2\text{O}_3$.

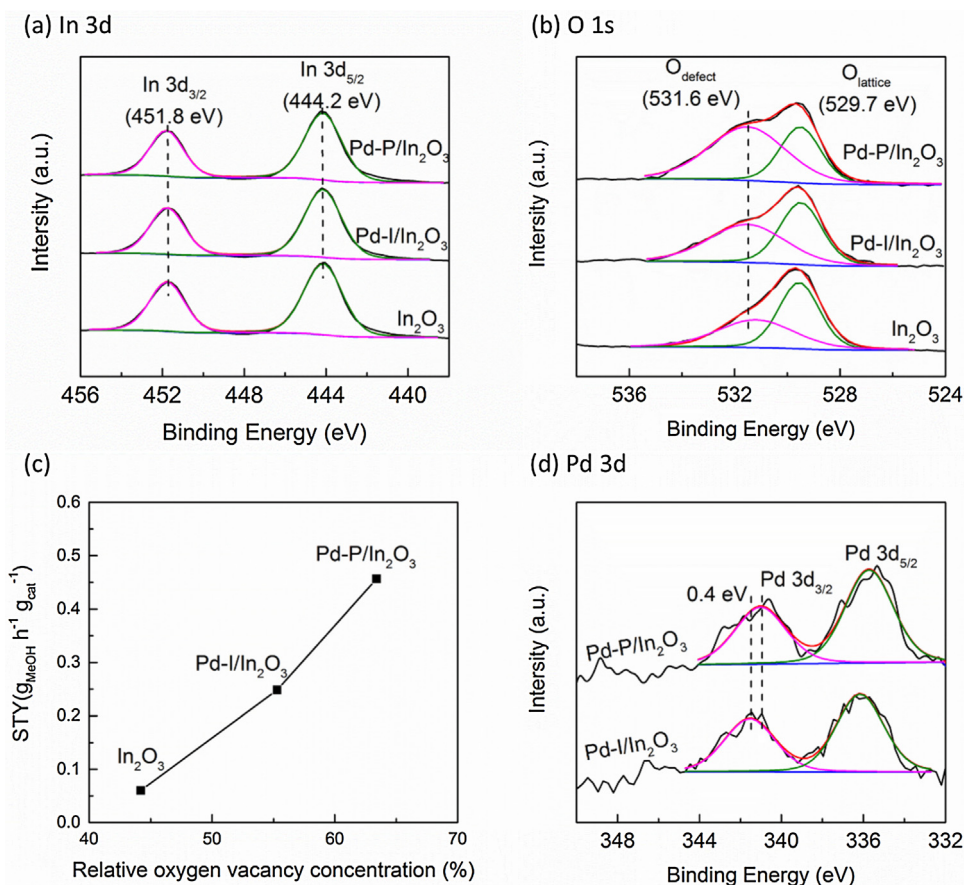


Fig. 8. The XPS spectra of (a) In 3d, (b) O 1s, and (d) Pd 3d of In_2O_3 and $\text{Pd/In}_2\text{O}_3$; (c) plot of the methanol STY at 250 °C as a function of the relative oxygen vacancy concentration.

of Pd^0 state (0.4 eV more than the shift of $\text{Pd-P/In}_2\text{O}_3$), indicating that the chemical environment of palladium has changed. The shift of $\text{Pd } 3d_{5/2}$ binding energy to higher energy can be attributed to the formation of Pd-In alloy [22,48], which is undesirable in CO_2 hydrogenation to methanol reaction due to the weak H_2 dissociation ability [20]. The greater shift of $\text{Pd-I/In}_2\text{O}_3$ implies more Pd-In alloy. To further verify the formation of Pd-In alloy, a plot of indium-to-palladium ratio (calculated by XPS result) before and after H_2 treatment is shown in Fig. S8(c). Before H_2 treatment, the relative Pd/In ratio of $\text{Pd-P/In}_2\text{O}_3$ is higher than that of $\text{Pd-I/In}_2\text{O}_3$, owing to the smaller particle size and better dispersion. After H_2 treatment, both In/Pd ratios increase. This can be explained by the formation of intermetallic Pd-In compounds and the diffusion of palladium into the bulk of the In_2O_3 support [22]. The In/Pd ratio of $\text{Pd-I/In}_2\text{O}_3$ is increasing more drastically, showing more Pd-In alloy formed during treatment. Therefore, using peptide as a stabilizer to control the size and dispersion of Pd NPs with electron reduction helps to prevent Pd-In alloy formation while the conventional incipient wetness impregnation preparation will not. This is consistent with the observation from XPS result in Fig. 8(d). The procedure of Pd-In alloy formation is shown in Fig. S8(d).

Our previous theoretical studies on In_2O_3 and In_2O_3 supported Pd cluster ($\text{Pd}_4/\text{In}_2\text{O}_3$) for CO_2 hydrogenation suggest: (1) In_2O_3 is a very good material for CO_2 adsorption and activation [49]. (2) More importantly, In_2O_3 can strongly enhance the selectivity for methanol production from CO_2 hydrogenation due to self-creation and self-healing of oxygen vacancies on In_2O_3 [16]. (3) $\text{Pd}_4/\text{In}_2\text{O}_3$ is predicted to be a promising catalyst for CO_2 hydrogenation to produce methanol, because the smaller Pd clusters are very active for H_2 dissociation, and the interfacial sites between the Pd cluster

and the support In_2O_3 cannot only activate CO_2 , but also facilitate H adatoms to react with CO_2 [19]. (4) The strong interaction between Pd and In results in the formation of Pd-In alloy during H_2 reduction, which exhibits weak ability for H_2 dissociation [20]. Due to reducibility of In_2O_3 , the H adatoms may affect the catalytic performance in two ways: reacting directly with the activated CO_2 or reducing In_2O_3 surface to create more oxygen vacancies. Weaker ability for H_2 dissociation of Pd-In alloy hampers the methanol yield, as few H adatoms will be generated to react with activated CO_2 and to produce few oxygen vacancy sites on the surface of In_2O_3 for CO_2 hydrogenation. Furthermore, the disappearance of the interfacial sites at $\text{Pd/In}_2\text{O}_3$ due to the Pd-In alloy formation also reduces the number of active sites available for CO_2 hydrogenation.

Moreover, we investigated the effect of the Pd particle size on the activity for methanol formation over $\text{Pd/In}_2\text{O}_3$ and compared the $\text{Pd-I/In}_2\text{O}_3$ and $\text{Pd-P/In}_2\text{O}_3$ catalysts with similar Pd loadings (around 1 wt.%) but with different Pd particle sizes (see Table 1).

Table 1
Physical properties of $\text{Pd/In}_2\text{O}_3$ catalysts.

Property	Catalysts	
	$\text{Pd-I/In}_2\text{O}_3$	$\text{Pd-P/In}_2\text{O}_3$
Pd loading ^a [%]	0.97	0.91
Pd diameter ^b [nm]	7.4	3.6
Dispersion ^c [%]	15.1	30.8
Pd surface atoms ^c [10^{19} atoms $\text{g}_{\text{cat}}^{-1}$]	8.3	15.9
Pd perimeter atoms ^c [10^{19} atoms $\text{g}_{\text{cat}}^{-1}$]	0.6	2.5

^a Measured by ICP-MS.

^b Measured by TEM.

^c Based on assuming half-spherical Pd particles.

Table 2Kinetic results and $\text{TOF}_{\text{Pd,surface}}$ and $\text{TOF}_{\text{Pd,perimeter}}$ values at 200 and 225 °C over the Pd/In₂O₃ catalysts.

Catalysts	MeOH yield [%]		MeOH formation rate [$10^{-7} \text{ mol s}^{-1} \text{ g}_{\text{cat}}^{-1}$]		$\text{TOF}_{\text{Pd,surface}}$ [10^{-4} s^{-1}]		$\text{TOF}_{\text{Pd,perimeter}}$ [10^{-4} s^{-1}]	
	200 °C	225 °C	200 °C	225 °C	200 °C	225 °C	200 °C	225 °C
Pd-I/In ₂ O ₃	0.36	1.43	1.9	7.4	13.5	53.9	16.9	67.4
Pd-P/In ₂ O ₃	0.79	3.18	4.1	16.7	15.5	63.4	8.9	36.4

Based on the distribution of the Pd particle sizes (Figure S3 and S6), we determined that the mean Pd particle sizes are 7.4 and 3.6 nm for the Pd-I/In₂O₃ and Pd-P/In₂O₃ catalysts, respectively. The number of Pd atoms on the surface and at the perimeter line of the particles was determined by assuming hemispherical Pd particles. The results were listed in Table 1.

The methanol yield and formation rate as a result of CO₂ hydrogenation are exhibited in Table 2 (200 and 225 °C). Both the methanol yield and formation rate increase significantly with the decreasing Pd particle size at 200 and 225 °C. These results demonstrated that the size of the Pd particles has a pronounced influence on the catalytic activity of the Pd/In₂O₃ catalysts for CO₂ hydrogenation to methanol.

Small particle sizes at a similar metal loading will result in increased number of particles, and therefore, more active sites for the formation of hydrogen adatoms [50]. Furthermore, more Pd NPs at smaller sizes are expected to generate more perimeter sites for CO₂ adsorption and hydrogenation. To determine which of the two reasons, hydrogen supply or number of the interfacial sites, contributes to the much improved performance for the smaller Pd NPs, we determined the turnover frequencies (TOFs) based on the number of surface Pd atoms ($\text{TOF}_{\text{Pd,surface}}$) and perimeter Pd atoms ($\text{TOF}_{\text{Pd,perimeter}}$) for different Pd/In₂O₃ catalysts (Table 2). For example, the $\text{TOF}_{\text{Pd,surface}}$ values at 200 °C are 13.5×10^{-4} and $15.2 \times 10^{-4} \text{ s}^{-1}$ for methanol formation over Pd particles of 7.4 and 3.6 nm, respectively. In contrast, for the perimeter atom based TOFs at the same temperature, $\text{TOF}_{\text{Pd,perimeter}}$ values are 16.9×10^{-4} and $8.9 \times 10^{-4} \text{ s}^{-1}$ over Pd particles of 7.4 and 3.6 nm, respectively. It decreases dramatically with the decreasing Pd particle size. These results indicate that the Pd NPs contribute to methanol production predominantly by generating H adatoms. The oxygen vacancy and Pd-In₂O₃ interfacial active sites are also responsible for the slightly increased TOFs with decreasing particle size.

The mechanism of methanol formation from CO₂ hydrogenation on In₂O₃ has been studied theoretically [16,49] and experimentally [18]. Previous results showed that CO₂ hydrogenation to a monodentate HCOO is both thermodynamically and kinetically favorable. Following a Mars van Krevelen mechanism, oxygen vacancy sites on the In₂O₃ surface assist both CO₂ activation and hydrogenation as well as stabilizing the key intermediates involved in methanol formation. Furthermore, the In₂O₃-based catalysts suppress the RWGS reaction by limiting surface COOH formation and steer the reaction to follow the formate route to methanol, as shown in the DFT study on Pd₄/In₂O₃ [19]. The present results also showed that the presence of the activated H adatoms on Pd NPs benefits methanol synthesis by lowering the activation barriers along the HCOO route. Interfacial sites between the Pd NPs and In₂O₃ can serve as active sites by activating CO₂ and facilitating the hydrogenation as well as spill the H adatoms over to the support. This is different from the reactions on the CZA catalyst, on which the COOH route competes with the HCOO pathway, and results in low selectivity toward methanol [51,52]. Therefore, the excellent performance of In₂O₃ and Pd/In₂O₃ catalyst is a result of enhanced stability of the key HCOO intermediates as well as the improved hydrogen supply. Consequently, the RWGS reaction is suppressed and the methanol formation becomes the dominant reaction pathway.

For Pd catalysts supported on metal-oxide surface, CO₂ reacts with hydrogen in a synergetic fashion: H₂ is dissociated on Pd particles and H adatoms spillover to adsorbed and activated CO₂ [53,54]. Therefore, both H₂ supply and activated CO₂ adsorption are important for CO₂ hydrogenation to methanol. To prepare the catalysts with balanced functions, we employed the peptide-assisted room temperature electron reduction to synthesize the Pd NPs in the form of Pd-P composite. The particle size of Pd NPs in this composite was controlled at ~2.0 nm with a narrow distribution. Characterization and testing of the Pd-P/In₂O₃ catalysts offer a much improved H₂ dissociation and selective CO₂ hydrogenation over the benchmark CZA catalyst, resulting in a highly selective CO₂ hydrogenation to methanol catalysts.

5. Conclusion

In this work, peptide was used to assist the preparation of the Pd/In₂O₃ catalyst by firstly mixing In₂O₃ powder with Pd/peptide composite and then removing peptide through thermal treatment. The resulting catalyst shows highly dispersed Pd NPs with particle size of 3.6 nm. Such Pd NPs exhibit significantly improved hydrogen dissociative adsorption ability, providing the needed hydrogen for hydrogenation reactions as well as maintaining the density of the oxygen vacancies. Both interfacial sites and the oxygen vacancy play important roles in the activation and hydrogenation of carbon dioxide to methanol. Enhanced CO₂ adsorption ability has been also achieved on the Pd/In₂O₃ catalysts, with Pd-P/In₂O₃ being more pronounced. All these lead to a superior performance of the Pd-P/In₂O₃ catalyst for CO₂ hydrogenation to methanol, with CO₂ conversion above 20%, methanol selectivity above 70% and STY up to $0.89 \text{ g}_{\text{MeOH}} \text{ h}^{-1} \text{ g}_{\text{cat}}^{-1}$ at 300 °C and 5 MPa. The activity is higher than that of the reported Cu- and Pd- based catalysts in literature. In addition, the Pd/In₂O₃ catalysts show an increased visible light absorption, suggesting a potential application in visible light photocatalysis.

Acknowledgements

This work was supported by the National Key Research and Development Program of China (2016YFB0600900) and the National Natural Science Foundation of China (21536008 and 21621004).

Appendix A. Supplementary data

Supplementary data associated with this article can be found, in the online version, at <http://dx.doi.org/10.1016/j.apcatb.2017.06.069>.

References

- [1] D. Jo, J. Bin Lim, T. Ryu, I.S. Nam, M.A. Camblor, S.B. Hong, Unseeded hydroxide-mediated synthesis and CO₂ adsorption properties of an aluminosilicate zeolite with the RTH topology, *J. Mater. Chem. A* 3 (2015) 19322–19329, <http://dx.doi.org/10.1039/c5ta03559g>.
- [2] N. Wang, K. Shen, L. Huang, X. Yu, W. Qian, W. Chu, Facile route for synthesizing ordered mesoporous Ni-Ce-Al oxide materials and their catalytic

- performance for methane dry reforming to hydrogen and syngas, *ACS Catal.* 3 (2013) 1638–1651, <http://dx.doi.org/10.1021/cs4003113>.
- [3] L. Liu, C. Zhao, J. Xu, Y. Li, Integrated CO₂ capture and photocatalytic conversion by a hybrid adsorbent/photocatalyst material, *Appl. Catal. B* 179 (2015) 489–499, <http://dx.doi.org/10.1016/j.apcatb.2015.06.006>.
 - [4] K. Sun, Z. Fan, J. Ye, J. Yan, Q. Ge, Y. Li, W. He, W. Yang, C. Liu, Hydrogenation of CO₂ to methanol over In₂O₃ catalyst, *J. CO₂ Util.* 12 (2015) 1–6, <http://dx.doi.org/10.1016/j.jcou.2015.09.002>.
 - [5] K. Chang, T. Wang, J.G. Chen, Hydrogenation of CO₂ to methanol over CuCeTiO_x catalysts, *Appl. Catal. B* 206 (2017) 704–711, <http://dx.doi.org/10.1016/j.apcatb.2017.01.076>.
 - [6] D. Masih, S. Rohani, J.N. Kondo, T. Tatsumi, Low-temperature methanol dehydration to dimethyl ether over various small-pore zeolites, *Appl. Catal. B* 217 (2017) 247–255, <http://dx.doi.org/10.1016/j.apcatb.2017.05.089>.
 - [7] J. Graciani, K. Mudiyanse, F. Xu, A.E. Baber, J. Evans, S.D. Senanayake, D.J. Stacchiola, P. Liu, J. Hrbeek, J.F. Sanz, J.A. Rodriguez, Highly active copper-ceria and copper-ceria-titania catalysts for methanol synthesis from CO₂, *Science* 345 (2014) 546–550, <http://dx.doi.org/10.1126/science.1253057>.
 - [8] J.A. Rodriguez, P. Liu, D.J. Stacchiola, S.D. Senanayake, M.G. White, J.G. Chen, Hydrogenation of CO₂ to methanol: importance of metal-oxide and metal-carbide interfaces in the activation of CO₂, *ACS Catal.* 5 (2015) 6696–6706, <http://dx.doi.org/10.1021/acscatal.5b01755>.
 - [9] H. Liu, T.D. Dao, L. Liu, X. Meng, T. Nagao, J. Ye, Light assisted CO₂ reduction with methane over group VIII metals: universality of metal localized surface plasmon resonance in reactant activation, *Appl. Catal. B* 209 (2017) 183–189, <http://dx.doi.org/10.1016/j.apcatb.2017.02.080>.
 - [10] X. Dong, F. Li, N. Zhao, F. Xiao, J. Wang, Y. Tan, CO₂ hydrogenation to methanol over Cu/ZnO/ZrO₂ catalysts prepared by precipitation-reduction method, *Appl. Catal. B* 191 (2016) 8–17, <http://dx.doi.org/10.1016/j.apcatb.2016.03.014>.
 - [11] F. Studt, M. Behrens, E.L. Kunkes, N. Thomas, S. Zander, A. Tarasov, J. Schumann, E. Frei, J.B. Varley, F. Abild-Pedersen, J.K. Nørskov, R. Schlögl, The mechanism of CO and CO₂ hydrogenation to methanol over Cu-based catalysts, *ChemCatChem* 7 (2015) 1105–1111, <http://dx.doi.org/10.1002/cctc.201500123>.
 - [12] Y. Xu, Y. Jia, Y. Zhang, R. Nie, Z. Zhu, J. Wang, H. Jing, Photoelectrocatalytic reduction of CO₂ to methanol over the multi-functionalized TiO₂ photocathodes, *Appl. Catal. B* 205 (2017) 254–261, <http://dx.doi.org/10.1016/j.apcatb.2016.12.039>.
 - [13] X. Jiang, N. Koizumi, X.W. Guo, C.S. Song, Bimetallic Pd-Cu catalysts for selective CO₂ hydrogenation to methanol, *Appl. Catal. B* 170 (2015) 173–185, <http://dx.doi.org/10.1016/j.apcatb.2015.01.010>.
 - [14] K. Siriwararata, V. Deetrakraka, P. Dittanetb, P. Kongkachuichay, Production of methanol from carbon dioxide using palladium-copper-zinc loaded on MCM-41: Comparison of catalysts synthesized from flame spray pyrolysis and sol-gel method using silica source from rice husk ash, *J. Clean. Prod.* 142 (2017) 1234–1243, <http://dx.doi.org/10.1016/j.jclepro.2016.07.099>.
 - [15] J. Ye, C. Liu, Q. Ge, A DFT study of methanol dehydrogenation on the PdIn(110) surface, *Phys. Chem. Chem. Phys.* 14 (2012) 16660–16667, <http://dx.doi.org/10.1039/C2CP42183F>.
 - [16] J. Ye, C. Liu, D. Mei, Q. Ge, Active oxygen vacancy site for methanol synthesis from CO₂ hydrogenation on In₂O₃(110): a DFT Study, *ACS Catal.* 3 (2013) 1296–1306, <http://dx.doi.org/10.1021/cs400132a>.
 - [17] T. Bielez, H. Lorenz, W. Jochum, R. Kaindl, F. Klausner, B. Klötzer, S. Penner, Hydrogen on In₂O₃: reducibility, non-doping, defect formation, and reactivity, *J. Phys. Chem. C* 114 (2010) 9022–9029, <http://dx.doi.org/10.1021/jp1017423>.
 - [18] O. Martin, A.J. Martin, C. Mondelli, S. Mitchell, T.F. Segawa, R. Hauert, C. Drouilly, D. Curulla-Ferré, J. Pérez-Ramírez, Indium oxide as a superior catalyst for methanol synthesis by CO₂ hydrogenation, *Angew. Chem. Int. Ed.* 55 (2016) 6261–6265, <http://dx.doi.org/10.1002/anie.201600943>.
 - [19] J. Ye, C. Liu, D. Mei, Q. Ge, Methanol synthesis from CO₂ hydrogenation over a Pd₄/In₂O₃ model catalyst: a combined DFT and kinetic study, *J. Catal.* 317 (2014) 44–53, <http://dx.doi.org/10.1016/j.jcat.2014.06.002>.
 - [20] J. Ye, Q. Ge, C. Liu, Effect of PdIn bimetallic particle formation on CO₂ reduction over the Pd-In/SiO₂ catalyst, *Chem. Eng. Sci.* 135 (2015) 193–201, <http://dx.doi.org/10.1016/j.ces.2015.04.034>.
 - [21] H. Lorenz, S. Turner, O.I. Lebedev, G. Van Tendeloo, B. Klötzer, C. Rameshan, K. Pfaller, S. Penner, Pd-In₂O₃ interaction due to reduction in hydrogen: consequences for methanol steam reforming, *Appl. Catal. A* 374 (2010) 180–188, <http://dx.doi.org/10.1016/j.apcata.2009.12.007>.
 - [22] M. Neumann, D. Teschner, A. Knop-Gericke, W. Reschtlowski, M. Armbrüster, Controlled synthesis and catalytic properties of supported In-Pd intermetallic compounds, *J. Catal.* 340 (2016) 49–59, <http://dx.doi.org/10.1016/j.jcat.2016.05.006>.
 - [23] W. Wang, C.F. Anderson, Z. Wang, W. Wu, H. Cui, C.-J. Liu, Peptide-templated noble metal catalysts: syntheses and applications, *Chem. Sci.* 8 (2017) 3310–3324, <http://dx.doi.org/10.1039/C7SC00069C>.
 - [24] J. Yan, Y. Pan, A.G. Cheetham, Y.-A. Lin, W. Wang, H. Cui, C.-J. Liu, One-step fabrication of self-assembled peptide thin films with highly dispersed noble metal nanoparticles, *Langmuir* 29 (2013) 16051–16057, <http://dx.doi.org/10.1021/la4036908>.
 - [25] Y.-X. Pan, H.-P. Cong, Y.-L. Men, S. Xin, Z.-Q. Sun, C.-J. Liu, S.-H. Yu, Peptide self-assembled biofilm with unique electron transfer flexibility for highly efficient visible-light-driven photocatalysis, *ACS Nano* 9 (2015) 11258–11265, <http://dx.doi.org/10.1021/acsnano.5b04884>.
 - [26] W. Wang, Z. Wang, M. Yang, C.-J. Zhong, C.-J. Liu, Highly active and stable Pt (111) catalysts synthesized by peptide assisted room temperature electron reduction for oxygen reduction reaction, *Nano Energy* 25 (2016) 26–33, <http://dx.doi.org/10.1016/j.nanoen.2016.04.022>.
 - [27] Z. Wang, M. Li, W. Wang, M. Fang, Q. Sun, C. Liu, Floating silver film: a flexible surface-enhanced Raman spectroscopy substrate for direct liquid phase detection at gas-liquid interfaces, *Nano Res.* 9 (2016) 1148–1158, <http://dx.doi.org/10.1007/s12274-016-1009-x>.
 - [28] R. Gaikwad, A. Bansode, A. Urakawa, High-pressure advantages in stoichiometric hydrogenation of carbon dioxide to methanol, *J. Catal.* 343 (2016) 127–132, <http://dx.doi.org/10.1016/j.jcat.2016.02.005>.
 - [29] M.A. Khalily, O. Ustahuseyin, R. Garifullin, R. Genc, M.O. Guler, A supramolecular peptide nanofiber templated Pd nanocatalyst for efficient Suzuki coupling reactions under aqueous conditions, *Chem. Commun.* 48 (2012) 11358, <http://dx.doi.org/10.1039/c2cc36228g>.
 - [30] Y. He, J. Fan, J. Feng, C. Luo, P. Yang, D. Li, Pd nanoparticles on hydrotalcite as an efficient catalyst for partial hydrogenation of acetylene: effect of support acidic and basic properties, *J. Catal.* 331 (2015) 118–127, <http://dx.doi.org/10.1016/j.jcat.2015.08.012>.
 - [31] S. Akbayrak, M. Kaya, M. Volkan, S. Özkar, Palladium(0) nanoparticles supported on silica-coated cobalt ferrite: a highly active, magnetically isolable and reusable catalyst for hydrolytic dehydrogenation of ammonia borane, *Appl. Catal. B* 147 (2014) 387–393, <http://dx.doi.org/10.1016/j.apcatb.2013.09.023>.
 - [32] J. Ryu, S.-W. Kim, K. Kang, C.B. Park, Synthesis of diphenylalanine/cobalt oxide hybrid nanowires and their application to energy storage, *ACS Nano* 4 (2010) 159–164, <http://dx.doi.org/10.1021/nn901156w>.
 - [33] M. Li, Q. Sun, C. Liu, Preparation of floating Au/PVP film on water for a green and rapid extraction of gold ion, *ACS Sustain. Chem. Eng.* 4 (2016) 3255–3260, <http://dx.doi.org/10.1021/acssuschemeng.6b00305>.
 - [34] H. Zhu, Pd/CeO₂-TiO₂ catalyst for CO oxidation at low temperature: a TPR study with H₂ and CO as reducing agents, *J. Catal.* 225 (2004) 267–277, <http://dx.doi.org/10.1016/j.jcat.2004.04.006>.
 - [35] R. Prins, Hydrogen spillover. Facts and fiction, *Chem. Rev.* 112 (2012) 2714–2738, <http://dx.doi.org/10.1021/cr200346z>.
 - [36] M. Kaur, N. Jain, K. Sharma, S. Bhattacharya, M. Roy, A.K. Tyagi, S.K. Gupta, J.V. Yakhmi, Room-temperature H₂S gas sensing at ppb level by single crystal In₂O₃ whiskers, *Sens. Actuators B-Chem.* 133 (2008) 456–461, <http://dx.doi.org/10.1016/j.snb.2008.03.003>.
 - [37] H. Zhu, X. Wang, F. Yang, X. Yang, Template-Free, Surfactantless route to fabricate In(OH)₃ monocrystalline nanoarchitectures and their conversion to In₂O₃, *Cryst. Growth Des.* 8 (2008) 950–956, <http://dx.doi.org/10.1021/cg700850e>.
 - [38] A. Baszczuk, M. Jasierski, M. Nyk, J. Hanuza, M. Mączka, W. Stręk, Luminescence properties of europium activated SrIn₂O₄, *J. Alloys Compd.* 394 (2005) 88–92, <http://dx.doi.org/10.1016/j.jallcom.2004.11.009>.
 - [39] J. Gan, X. Lu, J. Wu, S. Xie, T. Zhai, M. Yu, Z. Zhang, Y. Mao, S.C.I. Wang, Y. Shen, Y. Tong, Oxygen vacancies promoting photoelectrochemical performance of In₂O₃ nanocubes, *Sci. Rep.* 3 (2013), <http://dx.doi.org/10.1038/srep01021>.
 - [40] W. Wang, Y. Zhang, Z. Wang, J. Yan, Q. Ge, C. Liu, Reverse water gas shift over In₂O₃-CeO₂ catalysts, *Catal. Today* 259 (2016) 402–408, <http://dx.doi.org/10.1016/j.cattod.2015.04.032>.
 - [41] S. Mahalingam, H. Abdullah, I. Ashaari, S. Shaari, A. Muchtar, Optical, morphology and electrical properties of In₂O₃ incorporating acid-treated single-walled carbon nanotubes based DSSC, *J. Phys. D: Appl. Phys.* 49 (2016) 075601, <http://dx.doi.org/10.1088/0022-3727/49/7/075601>.
 - [42] F. Lei, Y. Sun, K. Liu, S. Gao, L. Liang, B. Pan, Y. Xie, Oxygen vacancies confined in ultrathin indium oxide porous sheets for promoted visible-light water splitting, *J. Am. Chem. Soc.* 136 (2014) 6826–6829, <http://dx.doi.org/10.1021/ja501866r>.
 - [43] J. Gan, X. Lu, T. Zhai, Y. Zhao, S. Xie, Y. Mao, Y. Zhang, Y. Yang, Y. Tong, Vertically aligned In₂O₃ nanorods on FTO substrates for photoelectrochemical applications, *J. Mater. Chem.* 21 (2011) 14685, <http://dx.doi.org/10.1039/c1jm11774b>.
 - [44] S. Zhang, P. Song, H. Yan, Q. Wang, Self-assembled hierarchical Au-loaded In₂O₃ hollow microspheres with superior ethanol sensing properties, *Sens. Actuators B-Chem.* 231 (2016) 245–255, <http://dx.doi.org/10.1016/j.snb.2016.03.020>.
 - [45] M. Brun, A. Berthet, J.C. Bertolini, XPS, AES and auger parameter of Pd and PdO, *J. Electron Spectrosc.* 104 (1999) 55–60, [http://dx.doi.org/10.1016/S0368-2048\(98\)00312-0](http://dx.doi.org/10.1016/S0368-2048(98)00312-0).
 - [46] M.C. Militello, Palladium oxide (PdO) by XPS, *Surf. Sci. Spectra* 3 (1994) 395, <http://dx.doi.org/10.1116/1.1247784>.
 - [47] E.H. Voigt, A.J.M. Mens, O.L.J. Gijzen, J.W. Geus, XPS analysis of palladium oxide layers and particles, *Surf. Sci.* 350 (1996) 21–31, [http://dx.doi.org/10.1016/0039-6028\(96\)01028-X](http://dx.doi.org/10.1016/0039-6028(96)01028-X).
 - [48] T. Skála, K. Veltruská, M. Moroseac, I. Matolínová, G. Korotchenkov, V. Matolín, Study of Pd-In interaction during Pd deposition on pyrolytically prepared In₂O₃, *Appl. Surf. Sci.* 205 (2003) 196–205, [http://dx.doi.org/10.1016/S0169-4332\(02\)01060-7](http://dx.doi.org/10.1016/S0169-4332(02)01060-7).
 - [49] J. Ye, C. Liu, Q. Ge, DFT study of CO₂ adsorption and hydrogenation on the In₂O₃ surface, *J. Phys. Chem. C* 116 (2012) 7817–7825, <http://dx.doi.org/10.1021/jp3004773>.
 - [50] M.W. Tew, J.T. Miller, J.A. van Bokhoven, Particle size effect of hydride formation and surface hydrogen adsorption of nanosized palladium catalysts:

- L₃ edge vs K edge X-ray absorption spectroscopy, *J. Phys. Chem. C* 113 (2009) 15140–15147, <http://dx.doi.org/10.1021/jp902542f>.
- [51] M. Huš, V.D.B.C. Dasireddy, N. Strah Štefančič, B. Likozar, Mechanism, kinetics and thermodynamics of carbon dioxide hydrogenation to methanol on Cu/ZnAl₂O₄ spinel-type heterogeneous catalysts, *Appl. Catal. B* 207 (2017) 267–278, <http://dx.doi.org/10.1016/j.apcatb.2017.01.077>.
- [52] Y. Yang, J. Evans, J.A. Rodriguez, M.G. White, P. Liu, Fundamental studies of methanol synthesis from CO₂ hydrogenation on Cu(111), Cu clusters, and Cu/ZnO(0001–), *Phys. Chem. Chem. Phys.* 12 (2010) 9909, <http://dx.doi.org/10.1039/c001484b>.
- [53] S. Collins, M. Baltanas, A. Bonivardi, An infrared study of the intermediates of methanol synthesis from carbon dioxide over Pd/ β -GaO, *J. Catal.* 226 (2004) 410–421, <http://dx.doi.org/10.1016/j.jcat.2004.06.012>.
- [54] S.E. Collins, J.J. Delgado, C. Mira, J.J. Calvino, S. Bernal, D.L. Chiavassa, M.A. Baltanás, A.L. Bonivardi, The role of Pd–Ga bimetallic particles in the bifunctional mechanism of selective methanol synthesis via CO₂ hydrogenation on a Pd/Ga₂O₃ catalyst, *J. Catal.* 292 (2012) 90–98, <http://dx.doi.org/10.1016/j.jcat.2012.05.005>.